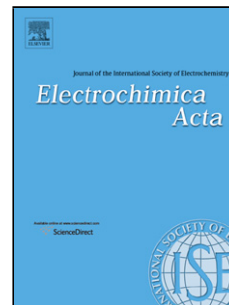


Accepted Manuscript

Title: Ni nanoparticle-decorated reduced graphene oxide for non-enzymatic glucose sensing: An experimental and modeling study

Authors: S. Darvishi, M. Souissi, F. Karimzadeh, M. Kharaziha, R. Sahara, S. Ahadian



PII: S0013-4686(17)30845-9
DOI: <http://dx.doi.org/doi:10.1016/j.electacta.2017.04.086>
Reference: EA 29343

To appear in: *Electrochimica Acta*

Received date: 10-2-2017
Revised date: 17-4-2017
Accepted date: 18-4-2017

Please cite this article as: S.Darvishi, M.Souissi, F.Karimzadeh, M.Kharaziha, R.Sahara, S.Ahadian, Ni nanoparticle-decorated reduced graphene oxide for non-enzymatic glucose sensing: An experimental and modeling study, *Electrochimica Acta*<http://dx.doi.org/10.1016/j.electacta.2017.04.086>

This is a PDF file of an unedited manuscript that has been accepted for publication. As a service to our customers we are providing this early version of the manuscript. The manuscript will undergo copyediting, typesetting, and review of the resulting proof before it is published in its final form. Please note that during the production process errors may be discovered which could affect the content, and all legal disclaimers that apply to the journal pertain.

Ni nanoparticle-decorated reduced graphene oxide for non-enzymatic glucose sensing: An experimental and modeling study

S. Darvishi¹, M. Souissi², F. Karimzadeh¹, M. Kharaziha¹, R. Sahara², S. Ahadian^{3,*}

¹Department of Materials Engineering, Isfahan University of Technology, Isfahan, Iran

²National Institute for Materials Science, Tsukuba, Japan

³Institute of Biomaterials and Biomedical Engineering, University of Toronto, Toronto, Canada

*Corresponding author: Institute of Biomaterials and Biomedical Engineering, University of Toronto, Toronto, Ontario M5S 3G9, Canada. Tel.: +1-416-946-5295. E-mail address: samad.ahadian@utoronto.ca.

Abstract

In this study, we used a facile approach to decorate Ni nanoparticles (Ni-NPs) with ethylene glycol followed by their adsorption on reduced graphene oxide (rGO) nanosheets for the development of enzyme free electrochemical glucose sensor. The effect of Ni-NP content (0.14, 0.28, 0.42, and 0.56 wt.%) on electrochemical properties and the molecular interaction of glucose with Ni-NPs/rGO in glucose sensing were evaluated. Ni-NPs/rGO showed significantly higher electrochemical performance for the glucose oxidation in alkaline solution compared to rGO. Specifically, 0.42% Ni-NPs/rGO revealed excellent performance for glucose determination with a wide linear range (0.25 μM to 1200 μM), a highly reproducible response and long-term stability with the calculated detection limit of 0.01 μM . Moreover, the reliability of the Ni-NPs/rGO sensor estimated using glucose concentration evaluation in human blood serum was confirmed. Ab initio calculations were employed to reveal molecular interactions of glucose with Ni-NPs/rGO. The results showed Ni₁₃ cluster with icosahedral geometry facing the graphene sheet is the most stable structure. Furthermore, the glucose molecule was able to adsorb on the graphene sheet through Ni₁₃ nanoclusters and the adsorption process is closely dependent on the orientation of Ni₁₃ nanoclusters.

Keywords: Sensor; Glucose; Ni nanoparticles; Non-enzymatic; Reduced graphene oxide.

1. Introduction

Glucose detection and monitoring are highly required for patients with diabetes. Different sensors with high sensitivity, superior reliability, and great selectivity have been employed for detection and monitoring of glucose level for patients [1, 2]. Electrochemical glucose sensors have been widely used due to its low cost, rapid and accurate measurements. In principal, these sensors are divided into two different types of enzymatic (based on glucose oxidase) and non-enzymatic sensors. Although enzymatic sensors have shown high glucose sensitivity and selectivity, they suffer from drawbacks including high cost, storage and operation in low temperatures (2-8 °C), and weak stability [3-5]. To overcome these issues, non-enzymatic glucose sensors based on nanomaterial-modified electrodes have been developed to allow direct oxidation of glucose on the nanomaterial surface. The nanomaterial-modified electrodes possess high sensibility, short response time, and low susceptibility to environmental parameters [6]. Large surface area of nanomaterials facilitates the electron transfer rate on the nanomaterial-modified electrodes. These nanomaterials can be metals and their alloys (*e.g.*, Pt, Au, Pd, and Cu) [6, 7], metal oxides (*e.g.*, Mn_xO_y [8], CuO [9], and Fe_3O_4 [10]), and carbon-based nanomaterials (*e.g.*, carbon nanotubes (CNTs) [11] and graphene (Gr) [12]). Among these nanomaterials, Gr as a two-dimensional and single-atom-thick nanomaterial with large surface area has been emerged as an ideal platform for sensing applications. Moreover, higher surface area of Gr nanosheets ($2630\text{ m}^2\cdot\text{g}^{-1}$) compared to that of graphite ($10\text{ m}^2\cdot\text{g}^{-1}$) and CNT ($1315\text{ m}^2\cdot\text{g}^{-1}$), exceptional ability to support fast electron-transfer kinetics, as well as functionalization capability make Gr an ideal platform for efficient nanoparticle immobilization. Based on these unique characteristics, integration of Gr nanosheets with metal and metal oxide nanoparticles has

been reported and widely been used to enhance the electrochemical characteristics of non-enzymatic glucose sensors [13].

Ni-based nanomaterials have shown good reversibility and excellent electrocatalytic oxidation of glucose [14]. Various types of Ni-based materials including NiO [15], Ni nanoparticles (Ni-NPs) [16], and NiOH [17] have been used alone or in the combination with carbon-based materials (*e.g.*, CNTs or Gr) for glucose detection. Ni-based sensors provide high-valent and oxyhydroxide components (NiOOH) in alkaline medium and thereby facilitate the oxidation process [18]. Although NiO and NiOH have excellent activity as electrode materials, their low electrical conductivity may lead to high internal resistance and poor performance in electrochemical devices. Compared to other types of Ni-based nanomaterials, Ni-NPs exhibit higher electrical conductivity, chemical stability, thermal resistance, and chemical activity [19].

Ni-NPs can be synthesized using various techniques, such as chemical reduction [20], sonochemical method [21], polyol process [22], and sol-gel method [23]. Among these methods, polyol process is a solvent-based technique in which a poly-alcohol, such as ethylene glycol (EG) is used as solvent and reducing agent. During in-situ oxidation of EG at a temperature closing to its boiling point, oxidation products consisting of acetaldehyde reduce precursor Ni ions to metallic nanoparticles. In order to prevent aggregation of metal nanoparticles in solution, a stabilizing agent is commonly used [23]. Recently, alkaline EG-based approach was developed in which NaOH provides OH groups on surface of nanoparticles leading to formation of stable metal nanoparticles without any surfactant [24]. This technique has been applied to synthesize various types of metallic nanoparticles consisting of rhodium, platinum, and ruthenium [25].

Several approaches have been employed to assemble Ni-NPs on surface of Gr nanosheets consisting of chemical vapor deposition [26], microwave irradiation [27], and electrochemical

deposition [28]. However, most of them require complicated and time-consuming procedures to prepare Ni-NPs/Gr materials. Recently, chemical reduction has been introduced as a convenient approach to synthesize Ni-NPs/rGO nanosheets [29]. The results demonstrated spontaneous redox between NiCl₂ and rGO nanosheets resulted in development of well-dispersed Ni-NPs. However, the efficiency of Ni reduction using technique was not sufficient [30]. Despite the use of Ni-NPs/Gr for non-enzymatic glucose detection, the effect of Ni-NP concentration on its electrocatalytic activity has not yet been evaluated. More importantly, molecular interaction of Ni-NPs with Gr in glucose detection process has not been studied.

Herein, we employed a simple and cost-effective polyol process to synthesize functionalized rGO nanosheets with Ni-NPs. In this technique, a combination of EG and hydrazine hydrate were used to make Ni-NPs/rGO nanosheets. Moreover, we evaluated the effect of Ni-NP concentration on glucose sensing of Ni-NPs/rGO nanosheets. Ab initio calculations were used to reveal molecular interactions of glucose with Ni-NPs/rGO.

2. Experimental procedure

2.1. Materials

Graphene oxide (GO) powder (thickness: 3.4-7 nm, purity>97%) was purchased from Nanosany Co, Iran. Ni chloride hexahydrate (NiCl₂.6H₂O, purity>98%), hydrazine hydrate (NH₂NH₂.H₂O, purity>99 %), extra pure sodium hydroxide (NaOH) pellets, glucose, EG (purity>99.8%), and ascorbic acid were obtained from Sigma-Aldrich, USA. Uric acid was purchased from Merck Co., Germany. Glassy carbon electrode (GCE) was prepared from Azar Electrode Co, Iran. Human blood serum samples were purchased from Health Clinic of Isfahan University of Technology.

2.2. Synthesis of Ni-NPs/rGO

Synthesis procedure of Ni-NPs/rGO is schematically shown in Fig. 1. GO and Ni precursor were separately prepared. To make Ni precursor, various amounts of Ni chloride (0.14, 0.28, 0.42, and 0.56 wt.%) were added to EG solution and stirred to obtain a homogenous green suspension. After heating the suspension at 60 °C for 1 h, 2.25 mL of hydrazine hydrate and sodium hydroxide (1 M) were added to it turning the solution color to black. After 1 h stirring at 60 °C, the reaction was completed based on the following equation:



GO powder was dispersed into deionized (DI) water using ultrasonication (Topsonics, 280 W and 20 kHz) for 1 h to prepare 0.5 mg/mL GO suspension. GO and Ni precursor solutions were then mixed and 20 mL hydrazine hydrate and 40 mg NaOH were added to the mixture followed by ultrasonication for 15 min. The mixture was refluxed at 100 °C for 5 h. After cooling at room temperature, as-synthesized solid products were collected by vacuum filtration, washed with DI water and ethanol for three times to remove excess chemicals. Lastly, the final product was dried in a vacuum oven at 60 °C for 24 h to obtain dried Ni-NPs/rGO. The samples were coded based on the Ni chloride concentration as 0.14, 0.28, 0.42, and 0.56% Ni-NPs/rGO.

2.3. Characterization of Ni-NPs/rGO

The chemical composition of Ni-NPs/rGO, Ni-NPs, and pure rGO nanosheets was revealed using X-ray diffraction (XRD, Philips, Holland) with Ni filtered $\text{CuK}\alpha$ ($\lambda = 1.5405 \text{ \AA}$) radiation. The average crystallite size (d) of Ni-NPs was calculated from the line broadening using the Scherrer's equation (Eq. 2):

$$d = k\lambda/\beta\cos\theta \quad (2)$$

where k is a constant (~ 1), β is the full width at half maximum and θ is the Bragg's angle. Surface morphology of Ni-NPs/rGO, Ni-NPs, and pure rGO nanosheets was investigated

using field emission scanning electron microscopy (Mira 3-XMU, Czech). Before imaging, samples were sputter coated with a thin layer of gold. Functional groups of rGO nanosheets and Ni-NPs/rGO were identified using a Senterra Raman spectroscope (Bruker, Germany) equipped with a 785 nm laser. Fourier transform infrared (FTIR) spectroscopy was performed by Bruker Tensor 27 over a range of 400-4000 cm^{-1} with a resolution of 2 cm^{-1} to verify the chemical composition of Ni-NPs as well as rGO nanosheets and Ni-NPs/rGO. Particle size analyzing was investigated with dynamic light scattering (DLS) technique using Vasco particle size analyzer (Cordouan Technologies, France) to estimate the Ni particle size distribution. X-ray photoelectron spectroscopy (XPS) was carried out on an ESCALAB Mark II (VG Company, U.K.). The energies were calibrated as Fermi edge (Metal Ni) as 0.0 eV .

2.4. Electrochemical evaluation of Ni-NPs/rGO

10 μL of Ni-NPs/rGO in DI water (1 mg/mL) was deposited on GCEs (Fig. 1). Prior to the surface modification, the GCE was polished with 3, 1, and 0.05 μm alumina slurries and washed out with DI water. Electrochemical experiments including cyclic voltammetry (CV), electrochemical impedance spectroscopy (EIS), and differential pulse voltammetry (DPV) were carried out using an electrochemical work station (Parstat 2273, USA). Electrochemical measurements were performed in 0.1 M NaOH supporting electrolyte at room temperature using three-electrode system consisting of a KCl saturated calomel electrode as the reference electrode, a platinum sheet as the counter electrode, and the Ni-NPs/rGO on GCEs as the working electrode. A certain volume of glucose stock solution (0.25-1200 μM) was added into the electrochemical cell, and then the three-electrode system was inserted into the cell to investigate electrochemical behavior of Ni-NPs/rGO sensors.

2.5. Computational method

Density functional theory method implemented in Vienna ab initio simulation package was used for describing molecular interactions between glucose and Ni-NPs/rGO [31, 32]. A spin-polarized magnetic approach with generalized gradient approximation formulated by Perdew, Burke, and Ernzerhof [33] was employed for exchange and correlation energy calculations. A 20 Å of vacuum space was imposed as the periodic boundary condition to the model system to preclude interactions with its images. Neutral and charged Ni₁₃ nanoclusters with icosahedral geometry are highly symmetric clusters as all of them favor a D_{3d} structure, a distorted icosahedron [34, 35]. Therefore, the icosahedron Ni₁₃ nanocluster was selected to represent Ni molecule.

The pristine Gr sheet consisted of a super cell of 4 × 4 times the primitive cell of hexagonal Gr and contained 64 carbon atoms. Full ionic relaxation was performed for the structure with 7 × 7 × 1 k-points as the mesh grid of the Brillouin zone. The cutoff energy was 520 eV, while the convergence criteria on the total energy and interatomic forces were 10⁻⁵ eV and 10⁻² eVÅ⁻¹, respectively. The adsorption energy was given by the following expression:

$$\Delta E_{\text{ads}} = E(\text{Gr} + \text{Ni} + \text{glucose} + \text{EG}) - E(\text{Gr}) - E(\text{Ni}) - E(\text{glucose}) - E(\text{EG}) \quad (3)$$

Here, the adsorption energy (ΔE_{ads}) was obtained from total energy of Ni₁₃, glucose, and EG molecules adsorbed on pristine Gr subtracted from individually calculated energies of Ni₁₃ nanocluster, glucose, and EG. A negative value of adsorption energy indicates that the adsorption can occur, while a positive value shows that the adsorption is not possible.

3. Results and discussion

3.1. Characterization of Ni-NPs and Ni-NPs/rGO

XRD pattern of Ni-NPs (Fig. 2(a)) confirmed the synthesis of pure Ni having a face-centered cubic structure without any impurity. The crystallite size of Ni-NPs was 15.2±2 nm as estimated

by three peaks of (111), (200), and (220) planes and the Scherrer equation. FTIR spectrum of Ni-NPs (Fig. 2(b)) consisted of vibrational peaks in the range of 3000-3500 cm^{-1} corresponding to the stretches of Ni and O-H bond. Moreover, the peaks at 2929, 1620, 1454, 1405, 1035, and 530 cm^{-1} were attributed to EG functional groups [36] implying that EG remained on the surface of Ni-NPs. Basically, alkaline EG approach provides functional groups of EG and OH^- ions on the surfaces of nanoparticles preventing the Ni-NP aggregation without any organic stabilizing agent. Moreover, the interaction of OH groups with Ni atoms limited the particle size and improved the colloidal stability of nanoparticles. In addition to purity, electrochemical properties of nanomaterials can be influenced by their shape and particle size distribution [37]. SEM image of Ni-NPs (Fig. 2(c)) demonstrated that as-synthesized nanoparticles consisted of spherical particles linked together to form chains of clusters due to strong interactions among magnetic dipoles of Ni-NPs. Based on the DLS analysis (Fig. 2(d)), Ni-NPs contained a homogenous size distribution in the range of 20 ± 0.2 nm.

XRD patterns (Fig. 3(a)) revealed that the most intensive peak of GO corresponded to (001) lattice plane at $2\theta = 11.7^\circ$ was disappeared for the rGO and Ni-NPs/rGO patterns confirming the reduction of GO. Based on a previous report, this peak with d-spacing around 0.79 nm is related to GO sheet interlayer spacing due to the presence of oxygen-containing groups and water molecules [38]. Moreover, the presence of two broad diffraction peaks at XRD pattern of rGO centered at $2\theta = 26.8^\circ$ and 54.7° corresponding to (002) and (100) lattice planes of rGO nanosheets confirmed successful reduction of GO. XRD patterns of Ni-NPs/rGO consisted of three diffraction peaks positioned at $2\theta = 44.4^\circ$, 51.8° , and 76.3° . These peaks were related to (111), (200), and (220) lattice planes of FCC Ni, respectively, confirming a complete reduction of rGO nanosheets and decoration of Ni-NPs on them. When GO sheet solution was dispersed in

Ni solution, Ni-NPs with EG functional groups were selectively bonded with carboxyl groups via electrostatic interactions. Through continuous stirring, the interlayer spacing between GO nanosheets helped the Ni-NPs to easily interlaminate into the enlarged layer. Following the addition of hydrazine hydrate, while GO nanosheets were reduced to rGO, Ni-NPs were continually grown onto rGO nanosheets.

Reduction of GO and interaction between rGO nanosheets and Ni-NPs were demonstrated using Raman spectroscopy (Fig. 3(b)). Raman spectrum of Gr was characterized by two main peaks: the G mode arising from the first-order scattering of E^{2g} phonon of sp^2 C atoms and the D mode arising from a breathing mode of k-point photons of A^{1g} symmetry [39]. Based on our results, GO consisted of a D band at 1355 cm^{-1} and a G band at 1590 cm^{-1} , which were shifted to lower numbers (1305 cm^{-1} and 1579 cm^{-1} , respectively) for rGO nanosheets (Supplementary Table S1) confirming the reduction of GO to rGO. In addition, D and G bands of Ni-NPs/rGO were at $1302\text{-}1308\text{ cm}^{-1}$ and $1580\text{-}1587\text{ cm}^{-1}$ ranges, respectively, depending on the Ni-NPs content (Supplementary Table S1). Such shifting towards lower wavelengths demonstrates the charge transfer between rGO and Ni-NPs [40]. In other words, the intensity ratio of the D and G band (I_D/I_G) is useful to evaluate ordered and disordered carbons [41]. According to the Table S1, I_D/I_G was increased from 1.7 for GO to 2.1 for rGO, which can be attributed to the restoration of numerous graphitic domains in the reduction process [42]. Moreover, the I_D/I_G for Ni-NPs/rGO was increased compared to that for GO suggesting a decrease in the size of in-plane sp^2 domains and a spatially ordered crystal structure of rGO as a result of Ni-NPs assembly onto rGO nanosheets [43].

FTIR spectra of GO, rGO, and Ni-NPs/rGO (Supplementary Fig. S1) demonstrated the presence of Ni-NPs and rGO nanosheets and their interactions. The broad absorption peaks

positioned at ~ 3445 and 1340 cm^{-1} were assigned to hydroxyl groups of water. Moreover, FTIR spectrum of GO consisted of peaks centered at 2957 , 2923 , 2854 cm^{-1} (CH_2 and CH_3 stretching), 1723 cm^{-1} (stretching mode of $\text{C}=\text{O}$), 1630 cm^{-1} (stretching mode of $\text{C}=\text{C}$), 1168 ($\text{C}-\text{OH}$ stretching), and 1031 cm^{-1} ($\text{C}-\text{O}-\text{C}$ stretching) [44]. After hydrazine reduction of GO and synthesis of Ni-NPs/rGO, the intensity of O-H band at 1340 cm^{-1} (denoted by a black dashed line) was significantly reduced and other characteristic peaks ($\text{C}=\text{O}$, $\text{C}-\text{OH}$, and $\text{C}-\text{O}-\text{C}$) were removed (shown by black arrows) demonstrating the reduction of GO in the presence of hydrazine [45]. Moreover, FTIR spectra of Ni-NPs/rGO consisted of two absorption bands centered at 2918 and 1620 cm^{-1} corresponded to EG confirming the successful functionalization of Ni-NPs.

Surface morphology and EDS-mapping of 0.42% Ni-NPs/rGO (Fig. 3(c) and Fig. 3(d), respectively) indicated a uniform distribution of Ni-NPs onto rGO nanosheets. Higher magnification image also revealed the presence of spherical-like Ni-NPs on wrinkly rGO nanosheets. Aggregation of Ni-NPs on rGO nanosheets was lower than that of pure Ni-NPs. Moreover, EDS spectrum (Fig. 3(d)) revealed that 0.42% Ni-NPs/rGO was composed of Ni, C, and O elements without any impurity from precursors. Increasing the concentration of Ni precursor up to 0.56 wt.% resulted in the agglomeration and formation of highly dense clusters of Ni-NPs on rGO nanosheets (Supplementary Fig. S2).

The elemental composition of Ni-rGO (0.56 wt% Ni) was revealed using XPS to characterize the oxidation state of Ni in the rGO system. Fig. 4(a) presents the survey spectrum of the XPS analysis. The percentage of individual elements based on XPS analysis is listed in Table 1. The survey spectra show the presence of C, O, and Ni. Some contaminants, such as N (NH_3), Na (NaCl), and Cl (NaCl) were also observed. The C 1s

XPS spectrum (Fig. 4(b)) has two peaks within a binding energy range between 282 eV and 292 eV. The O 1s XPS spectrum (Fig. 4(c)) shows three components: NiO (529.6 eV), Ni₂O₃ state with main strong peak around 531.6 eV, and the third component has a peak around 532.7 eV and it is an overlap between C-OH, C-O (GO), C=O, and COOH states. In the Ni 2p spectrum (Fig. 4(d)), a low binding energy of metallic Ni state is observed, as compared to Ni 2p_{1/2} and Ni 2p_{3/2} states.

High-resolution XPS spectra deconvolution of the C 1s core-level (Fig. 4(e)) shows five distinct peaks corresponding to different types of C components: the sp²-hybridized C-C (284.5 eV), the C with the dangling OH groups C-OH (285.9 eV), C-O-O (GO) (287.1 eV), the carbonyls CO (288.3 eV), COOH (289.4 eV), in consistence with the XPS spectra reported by Kundu et al. [46], and a not clearly recognizable compound –O-C=O-O– at 290.5 eV. The decomposition of Ni 2p_{3/2} XPS spectra, shown in Fig.4(f), indicates four different peaks corresponding to three distinct bonding states of Ni in the rGO adsorbed Ni-NPs: metallic Ni (852.7 eV) with satellite peak around 861.6 eV, Ni(II) oxide NiO (853.8 eV), and Ni(III) oxide Ni₂O₃, around 856.2 eV. This indicates that Ni²⁺ and Ni³⁺ states are highly involved in the O reduction on the rGO surface. On the other hand, the peak of NiO state may overlap with those of Ni(OH)₂ and NiO(OH), as all the three have multiplet structures and close binding energies [47]. We found that the ratio of metal Ni and hydroxide NiOH is about 1:9, and a strong peak revealing that the main bonding state of Ni in the rGO was through formation of Ni₂O₃.

3.2. Electrochemical evaluation of Ni-NPs/rGO

Electrochemical performance of Ni-NPs, rGO, and Ni-NPs/rGO on a GCE was evaluated

using CV, DPV, and EIS measurements. In the absence of glucose, bare GCE and rGO did not show any redox peak in working potential range (Fig. 5(a)). The CV curve of Ni-NPs in 0.1 M NaOH solution at the scan rate of 50 mV s⁻¹ (Fig. 5(a)) consisted of a pair of well-defined redox peaks with an anodic peak at 0.46 V and a cathodic peak at 0.27 V. These peaks were corresponded to an electrochemical transform between NiOOH and Ni(OH)₂ (Ni(II)/Ni(III) redox couple), mainly governed by the Faradaic redox mechanism.

After introducing Ni-NPs onto rGO nanosheets, well-defined broad redox reaction peaks at around 0.54 V (oxidation peak) and 0.25 V (reduction peak), respectively were visible in the CV curves of Ni-NPs/rGO (Fig. 5(b)). In addition, the current outputs at the redox peaks were higher than those for Ni-NPs and rGO indicating enhanced electrical conductivity and facile ion transport in Ni-NPs/rGO.

Upon the addition of 1 mM glucose, the oxidation of glucose on bare and modified GCEs were evaluated using CV curves (Fig. 5(c)). No redox peak was observed in the CV curves of bare GCE and rGO electrodes suggest that glucose did not undergo the redox reaction. Compared to non-glucose condition, the oxidation reaction of glucose on Ni-NPs revealed less positive potentials (about 0.4 V) confirming that Ni-NPs had redox peak in lower potentials in the presence of glucose (Fig. 5(c)). Furthermore, the anodic peak currents were significantly increased representing a major role of Ni-NPs in the oxidation of glucose. The electrochemical response of Ni-NPs to the glucose oxidation can be expressed as follows [48]:



Based on this mechanism, Ni(III) species were rapidly oxidized the glucose at the anode, which produced Ni(II) species. Furthermore, the catalytic oxidation of glucose was detected in the negative scan, until the surface reduction potential was reached and the surface became electro-catalytically inactive again.

The electrochemical response of Ni-NPs/rGO to glucose (Fig. 5(d)) was notably enriched compared to Ni-NPs because of synergistic effect of Ni-NPs and rGO nanosheets as well as improved conductivity and surface area of electrode. It has been shown that edge-plane-like defective sites on rGO provide active sites for electron transfer to biological species, such as glucose [49] (Schematic illustrating the electrochemical behavior of Ni-NPs/rGO sensor in the presence of glucose shown in Fig. 5(e)).

Nyquist diagrams of GCE, Ni-NPs, rGO, and Ni-NPs/rGO in 0.1 M KCl electrolyte solution containing 0.5 mM $\text{Fe}(\text{CN})_6^{3-}$ solution are presented in Fig. S3(a, b). These diagrams consisted of high frequency loops due to facile electron transfer on rGO, Ni-NPs, and Ni-NPs/rGO electrodes. The solution impedance value was near zero for all samples because of low resistance between working and reference electrodes. The diameter of circles in the Nyquist plots was decreased from rGO to Ni-NPs and finally to Ni-NPs/rGO as a result of an increase in electrode surface area revealing higher chemically active surface sites and formation of highly conductive Ni-NPs onto rGO nanosheets. Generally, Ni-NPs with high surface to volume ratio are a promising candidate for sensing applications [50, 51]. However, high affinity of Ni-NPs to agglomerate has decreased their sensing efficiency. On the other hand, high surface area of rGO could improve interfacial contact with other components [52]. Moreover, large surface of rGO could prevent the aggregation of secondary components. Therefore, large surface area of rGO as well as uniformly

distributed active sites of NPs make rGO-NPs structure appropriate for improvement of electrical conductivity of hybrids compared to pure Ni-NPs and rGO nanosheets.

However, the incorporation of more Ni-NPs (0.56% Ni-NPs/rGO) resulted in larger semicircle diameters mainly because of Ni-NP agglomeration and thereby a decrease in surface area and electrocatalytic behavior of electrodes. Charge transfer resistance (R_{ct}) is a key parameter to assess kinetics of a redox probe at electrode interface. R_{ct} values were decreased from 10543 Ω for bare GCE to 7234 Ω for rGO confirming the positive effect of rGO on electron transfer at the electrode surface. R_{ct} value was further decreased to 746 Ω for Ni-NPs demonstrating catalytic activity of Ni-NPs due to facile electron transfer by Ni(III)/Ni(II) redox couple. R_{ct} values were 28, 11, 4, and 21 Ω for 0.14, 0.28, 0.42 and 0.56 wt.% Ni-NPs on rGO indicating the assembly of Ni-NPs facilitated the electron transfer of the redox probe. rGO nanosheets not only provided more sites (edges and basal layer) for the immobilization of Ni-NPs, but also served as a template to prevent Ni-NPs aggregation leading to improved electron transfer properties.

Nyquist diagrams of Ni-NPs, rGO, and Ni-NPs/rGO in 0.1 M KCl electrolyte solution containing 0.5 mM $\text{Fe}(\text{CN})_6^{3-}$ and glucose are shown in Fig. S3(c, d). When the glucose was added the solutions, the diameter of semicircles was reduced. R_{ct} values were decreased from 608 Ω for GCE to 513, 21, 10.1, 3.2, and 18 Ω for rGO, 0.14% Ni-NPs/rGO, 0.28% Ni-NPs/rGO, 0.42% Ni-NPs/rGO, and 0.56% Ni-NPs/rGO respectively. The R_{ct} reduction can be attributed to reaction between the glucose and Ni-NPs causing the production of $\text{Ni}(\text{OH})_2$ in lower potentials at the electrode surface. Since 0.42% Ni-NPs/rGO had the best electrochemical behavior, it was selected for further electrochemical characterizations as follows.

DPV curves were recorded for 0.42% Ni-NPs/rGO in the presence of various concentrations of glucose (0.25-1200 μM) to obtain the calibration curve (Fig. 6). Our results demonstrated the detection of glucose over small concentrations of 0.01 μM . Previous researches similarly reported low concentrations of glucose detection (1 μM) when graphene-based nanomaterials were applied as sensors due to the presence of carboxyl acid functional groups [53-56]. According to the previous reports, glucose can covalently be attached to the carboxyl acid groups of GO leading to the enhancement in the glucose detection even at low concentrations [53]. It was also shown that the variation of DPV peak current versus the glucose concentration was linear. Ni-NPs/rGO exhibited a high sensitivity for the glucose detection ($0.0025 \text{ mA}\mu\text{M}^{-1}$) comparable to other glucose sensors with high sensitivity (Table S2). Limitation of detection (LOD) for our developed sensor was about 0.01 μM as determined using $\text{LOD}=3s_b/S$, where s_b is the standard deviation of blank measurement and S is derived from the calibration sensitivity and it is the slope of linear plot between concentration versus current. Among the sensors listed in Table S2, Zhang *et al.* [28] reported Ni-NPs grown on rGO nanosheets with a sensitivity of $10200 \mu\text{A}\cdot\mu\text{M}^{-1} \text{ cm}^{-2}$, higher sensitivity than our works, and LOD of 0.1 μM , higher than what we reported here. Compared to their work, our one step, less-expensive, and easy preparation method are the advantage of our system.

In order to investigate reproducibility and stability of Ni-NPs/rGO sensor, five continuous measurements of oxidation currents were performed on the same electrode of Ni-NPs/rGO in the solution of 0.1 M NaOH containing 0.7 mM glucose. A relative standard deviation (RSD) of 1.9% ($n=5$) confirmed that Ni-NPs/rGO has an excellent reproducibility for continuous glucose detection (Fig. S4(a)). In another set of experiment, five parallel Ni-NPs/rGO electrodes were

fabricated in the same experimental setup and then used to detect 0.7 mM glucose. RSD of 2.2% (n=5, after one month) was achieved in this assessment (Fig. S4(b)). These results strongly suggest that electrode fabrication process was reproducible and Ni-NPs/rGO sensors demonstrated high stability for repetitive detection of glucose.

Anti-references capability of Ni-NPs/rGO sensors (the ability of glucose differentiation from other species) was also evaluated. To this end, the voltammetry response of Ni-NPs/rGO was examined by detecting some co-existing electro-active species, such as ascorbic acid, ethanol, acetaminophen, and uric acid. Fig. S4 (c-f) shows the response of Ni-NPs/rGO electrode to 0.01 M ascorbic acid, 0.01 M ethanol, 0.01 M acetaminophen, and 0.01 M uric acid in the absence and presence of 0.05 mM glucose in 0.1 M NaOH solution, respectively. The glucose oxidation current in the absence of any interference was estimated around 0.16 mA at the Ni-NPs/rGO electrode (Fig. 5). The I_{G+I}/I_G , which is the ratio of current response of glucose in presence of interferences to the current response of glucose were 1.04, 2.8, 1.01 and 0.95 for uric acid, ascorbic acid, acetaminophen, and ethanol, respectively. Results demonstrated that uric acid, acetaminophen, and ethanol had no substantial change in the current response for 0.05 mM glucose in the presence of these interferences. Ascorbic acid caused a little interference to Ni-NPs/rGO electrode response to glucose, because it can be also electrocatalytically oxidized by Ni-NPs/rGO. Moreover, the potential peak for uric acid, ascorbic acid, and acetaminophen were about 0.415 V, -0.106 V, and 0.3 V, respectively. Compared to the glucose oxidation peak, potential differences between neighboring peaks were about 0.18 V, 0.7 V, and 0.2 V, which are large enough for a selective

determination of glucose in the existence of uric acid, ascorbic acid, and acetaminophen. The Ni-NPs/rGO electrode hadn't response to ethanol. As a result, Ni-NPs/rGO glucose sensor shows good selectivity for glucose detection.

Practical applicability of proposed sensor was investigated by determination of glucose in human blood serum samples (containing 4.5 mM glucose) (Fig. S4(g)). In this analysis, 1 mL of serum was introduced in an electrochemical cell containing 0.1 M of NaOH and the glucose content was measured using the proposed sensor and then compared with the value obtained using a conventional glucometer (81 mg/100 mL). The sensor showed 4.38 mM glucose in the cells, which was close to the data obtained from the glucometer. The RSD was 2.3%, showing high accuracy of the sensor to measure real sample. This result validates the potential use of our developed sensor for glucose detection in clinic.

3.3. Computational study of molecular interaction between Ni-NPs/rGO and Glucose

Calculated adsorption energies and electron localization function (ELF) [57] maps on (110) plan are summarized in Fig. 7 and Fig. S5. Local magnetic moments (μ_B) and Bader charges (q^B) [58, 59] of elemental species in each configuration are shown in Table 2 and Table 3, respectively. The Ni₁₃ cluster with icosahedral geometry can be adsorbed on the Gr sheet with three possible orientations namely, triangular facet facing the Gr, the bonding edge of atoms facing Gr, and the Ni₁₃ top atom facing Gr substrate. Among these configurations, Ni₁₃, which has the triangular facet of nanocluster facing the Gr was the most stable structure. A complete relaxation for all atoms of Ni₁₃ deposited on Gr resulted in the distortion of icosahedral geometry of Ni₁₃ nanocluster with a slight concave local distortion of sp²-bonded C atoms on the Gr (C-C distance increased from 1.42 to 1.44 Å, by about 1.4%).

Calculated adsorption energy (ΔE_{ads}) for the Ni₁₃ nanocluster adsorbed on Gr (Fig. 7(a)) was -1.81 eV, which is in consistence with previously reported value [60]. Fig. 7(b) shows the ELF plot for the (110) plane of Ni₁₃ nanocluster adsorbed on Gr in which a depletion of electrons on Ni₁₃ cluster and a polarized excess of electrons around the Gr sheet is obvious. This is consistent with the Bader charges indicating a charge loss of $-0.257e$ for Ni atoms and a gain of $+0.065e$ for C atoms (Table 3).

Each Ni atom in the triangular facet of Ni₁₃ nanocluster was bonded to two C atoms with a hexagonal ring of Gr, with the average Ni–C bond length of 2.08 Å. Table 2 shows that the local magnetic moment of Ni atom is reduced by 44%, from $0.615 \mu_{\text{B}}$ to $0.344 \mu_{\text{B}}$, as a result of bonding of Ni to C atoms. On the other hand, after introducing the glucose molecule to the system, we obtained the largest adsorption energy (-6.55 eV). The local magnetic moment of Ni atom was much reduced in this case, especially for the Ni atom, which was the nearest neighbor of Gr ($\sim 0.022 \mu_{\text{B}}$). This reduction of magnetic moment for Ni atoms is associated with a charge transfer, mainly, from C atoms of Gr and Ni atoms toward O atoms of glucose molecule. Using Bader charges analysis, we confirmed charge losses of $-0.469e$ for Ni and $-1.129e$ for C atom of Gr, with $+1.662e$ excess of charge on O atom of glucose. The ELF map of this system (Fig. 7(c)) shows a clear localization of electrons around the O of glucose and much less electrons located on top of Gr.

It is interesting to notice that the adsorption energy became larger as we changed the orientation of Ni₁₃ nanocluster from top of atom facing the EG to the triangular facet facing the EG interacting through a π - π bonding. In the former structure, we found large enhancement on the local magnetic moment of Ni atoms, indicating less stable configuration. However, the adsorption energy in the latter is larger, where the magnetic moment of Ni atoms was reduced,

accompanied by a charge flow transferred from C and Ni atoms toward the O atoms of the glucose. Local density of states of glucose adsorption on Gr (Fig. S6 and Fig. S7) further confirmed charge transfer among molecular species. Taken together, our ab initio results indicated two major insights. First, glucose molecule can be effectively adsorbed on Gr sheets via the assistance of Ni₁₃ nanoclusters and addition of EG. Second, this adsorption process is closely dependent on the orientation of Ni₁₃ nanoclusters.

4. Conclusions

In this work, we presented a non-enzymatic glucose sensor based on Ni-NPs and rGO nanosheets without any linker. Using a simple, efficient, and low-cost polyol method, GO was reduced to rGO, while Ni-NPs were simultaneously decorated on them. The results demonstrated uniform dispersion of Ni-NPs with an average size of 20 ± 0.2 nm onto the rGO sheets. The modified electrodes with Ni-NPs/rGO exhibited high electrochemical behavior and excellent electro-catalytic oxidation of glucose. While rGO played a role as a nucleation center and template for in situ growth of Ni-NPs, the synergistic effect of rGO with Ni-NPs improved the electrochemical behavior of pure Ni-NPs. Our computational results also revealed molecular interaction of species for glucose detection.

Acknowledgments

The authors are grateful for support of this research by Isfahan University of Technology, Iran and Mr. Hirohito Ohata in the Materials Analysis Station for performing the XPS measurements and analysis at National Institute for Materials Science (NIMS), Japan.

References

- [1] E. Crouch, D.C. Cowell, S. Hoskins, R.W. Pittson, J.P. Hart, A novel, disposable, screen-printed amperometric biosensor for glucose in serum fabricated using a water-based carbon ink, *Biosensors and Bioelectronics*, 21 (2005) 712-718.
- [2] E.-H. Yoo, S.-Y. Lee, Glucose biosensors: an overview of use in clinical practice, *Sensors*, 10 (2010) 4558-4576.
- [3] M.S.-P. López, D. Mecerreyes, E. López-Cabarcos, B. López-Ruiz, Amperometric glucose biosensor based on polymerized ionic liquid microparticles, *Biosensors and Bioelectronics*, 21 (2006) 2320-2328.
- [4] H. Muguruma, Y. Kase, Structure and biosensor characteristics of complex between glucose oxidase and plasma-polymerized nanothin film, *Biosensors and Bioelectronics*, 22 (2006) 737-743.
- [5] R. Nenkova, D. Ivanova, J. Vladimirova, T. Godjevargova, New amperometric glucose biosensor based on cross-linking of glucose oxidase on silica gel/multiwalled carbon nanotubes/polyacrylonitrile nanocomposite film, *Sensors and Actuators B: Chemical*, 148 (2010) 59-65.
- [6] K. Tian, M. Prestgard, A. Tiwari, A review of recent advances in nonenzymatic glucose sensors, *Materials Science and Engineering: C*, 41 (2014) 100-118.
- [7] Y. Lv, S. Jin, Y. Wang, Z. Lun, C. Xia, Recent advances in the application of nanomaterials in enzymatic glucose sensors, *Journal of the Iranian Chemical Society*, 13 (2016) 1767-1776.
- [8] L. Han, C. Shao, B. Liang, A. Liu, Genetically Engineered Phage-Templated MnO₂ Nanowires: Synthesis and Their Application in Electrochemical Glucose Biosensor Operated at Neutral pH Condition, *ACS applied materials & interfaces*, (2016).
- [9] Y.-W. Hsu, T.-K. Hsu, C.-L. Sun, Y.-T. Nien, N.-W. Pu, M.-D. Ger, Synthesis of CuO/graphene nanocomposites for nonenzymatic electrochemical glucose biosensor applications, *Electrochimica Acta*, 82 (2012) 152-157.
- [10] L. Yang, X. Ren, F. Tang, L. Zhang, A practical glucose biosensor based on Fe₃O₄ nanoparticles and chitosan/nafiion composite film, *Biosensors and Bioelectronics*, 25 (2009) 889-895.
- [11] Y. Liu, M. Wang, F. Zhao, Z. Xu, S. Dong, The direct electron transfer of glucose oxidase and glucose biosensor based on carbon nanotubes/chitosan matrix, *Biosensors and Bioelectronics*, 21 (2005) 984-988.
- [12] M. Liu, R. Liu, W. Chen, Graphene wrapped Cu₂O nanocubes: non-enzymatic electrochemical sensors for the detection of glucose and hydrogen peroxide with enhanced stability, *Biosensors and Bioelectronics*, 45 (2013) 206-212.
- [13] J.C. Claussen, A. Kumar, D.B. Jaroch, M.H. Khawaja, A.B. Hibbard, D.M. Porterfield, T.S. Fisher, Nanostructuring platinum nanoparticles on multilayered graphene petal nanosheets for electrochemical biosensing, *Advanced Functional Materials*, 22 (2012) 3399-3405.
- [14] K.E. Toghill, L. Xiao, M.A. Phillips, R.G. Compton, The non-enzymatic determination of glucose using an electrolytically fabricated nickel microparticle modified boron-doped diamond electrode or nickel foil electrode, *Sensors and Actuators B: Chemical*, 147 (2010) 642-652.

- [15] A. Salimi, E. Sharifi, A. Noorbakhsh, S. Soltanian, Immobilization of glucose oxidase on electrodeposited nickel oxide nanoparticles: direct electron transfer and electrocatalytic activity, *Biosensors and Bioelectronics*, 22 (2007) 3146-3153.
- [16] H. Nie, Z. Yao, X. Zhou, Z. Yang, S. Huang, Nonenzymatic electrochemical detection of glucose using well-distributed nickel nanoparticles on straight multi-walled carbon nanotubes, *Biosensors and Bioelectronics*, 30 (2011) 28-34.
- [17] G. Yang, E. Liu, N.W. Khun, S.P. Jiang, Direct electrochemical response of glucose at nickel-doped diamond like carbon thin film electrodes, *Journal of Electroanalytical Chemistry*, 627 (2009) 51-57.
- [18] L.-M. Lu, L. Zhang, F.-L. Qu, H.-X. Lu, X.-B. Zhang, Z.-S. Wu, S.-Y. Huan, Q.-A. Wang, G.-L. Shen, R.-Q. Yu, A nano-Ni based ultrasensitive nonenzymatic electrochemical sensor for glucose: enhancing sensitivity through a nanowire array strategy, *Biosensors and Bioelectronics*, 25 (2009) 218-223.
- [19] N. Cordente, M. Respaud, F. Senocq, M.-J. Casanove, C. Amiens, B. Chaudret, Synthesis and magnetic properties of nickel nanorods, *Nano letters*, 1 (2001) 565-568.
- [20] Z.G. Wu, M. Munoz, O. Montero, The synthesis of nickel nanoparticles by hydrazine reduction, *Advanced Powder Technology*, 21 (2010) 165-168.
- [21] S.M. Meybodi, S. Hosseini, M. Rezaee, S. Sadrnezhad, D. Mohammadyani, Synthesis of wide band gap nanocrystalline NiO powder via a sonochemical method, *Ultrasonics sonochemistry*, 19 (2012) 841-845.
- [22] G.G. Couto, J.J. Klein, W.H. Schreiner, D.H. Mosca, A.J. de Oliveira, A.J. Zarbin, Nickel nanoparticles obtained by a modified polyol process: synthesis, characterization, and magnetic properties, *Journal of colloid and Interface science*, 311 (2007) 461-468.
- [23] D.-H. Chen, X.-R. He, Synthesis of nickel ferrite nanoparticles by sol-gel method, *Materials Research Bulletin*, 36 (2001) 1369-1377.
- [24] H. Kawasaki, Surfactant-free solution-based synthesis of metallic nanoparticles toward efficient use of the nanoparticles' surfaces and their application in catalysis and chemo-/biosensing, *Nanotechnology Reviews*, 2 (2013) 5-25.
- [25] Y. Wang, J. Ren, K. Deng, L. Gui, Y. Tang, Preparation of tractable platinum, rhodium, and ruthenium nanoclusters with small particle size in organic media, *Chemistry of Materials*, 12 (2000) 1622-1627.
- [26] Y. Zhang, L. Gomez, F.N. Ishikawa, A. Madaria, K. Ryu, C. Wang, A. Badmaev, C. Zhou, Comparison of graphene growth on single-crystalline and polycrystalline Ni by chemical vapor deposition, *The Journal of Physical Chemistry Letters*, 1 (2010) 3101-3107.
- [27] Z. Wang, Y. Hu, W. Yang, M. Zhou, X. Hu, Facile one-step microwave-assisted route towards Ni nanospheres/reduced graphene oxide hybrids for non-enzymatic glucose sensing, *Sensors*, 12 (2012) 4860-4869.
- [28] Y. Zhang, X. Xiao, Y. Sun, Y. Shi, H. Dai, P. Ni, J. Hu, Z. Li, Y. Song, L. Wang, Electrochemical deposition of nickel nanoparticles on reduced graphene oxide film for nonenzymatic glucose sensing, *Electroanalysis*, 25 (2013) 959-966.
- [29] W. Lu, X. Qin, A.M. Asiri, A.O. Al-Youbi, X. Sun, Facile synthesis of novel Ni (II)-based metal-organic coordination polymer nanoparticle/reduced graphene oxide nanocomposites and their application for highly sensitive and selective nonenzymatic glucose sensing, *Analyst*, 138 (2013) 429-433.

- [30] B. Wang, S. Li, J. Liu, M. Yu, Preparation of nickel nanoparticle/graphene composites for non-enzymatic electrochemical glucose biosensor applications, *Materials Research Bulletin*, 49 (2014) 521-524.
- [31] G. Kresse, J. Furthmüller, Efficiency of ab-initio total energy calculations for metals and semiconductors using a plane-wave basis set, *Computational Materials Science*, 6 (1996) 15-50.
- [32] G. Kresse, D. Joubert, From ultrasoft pseudopotentials to the projector augmented-wave method, *Physical Review B*, 59 (1999) 1758.
- [33] J.P. Perdew, K. Burke, M. Ernzerhof, Generalized gradient approximation made simple, *Physical review letters*, 77 (1996) 3865.
- [34] F. Reuse, S. Khanna, S. Bernel, Electronic structure and magnetic behavior of Ni 13 clusters, *Physical Review B*, 52 (1995) R11650.
- [35] X. Zun, M. Qing-Min, W. Jing, L. Ying, L. You-Cheng, Effects of charge on the structures and spin moments of Ni₁₃ cluster, *Chinese Physics*, 16 (2007) 3637.
- [36] W. Sawodny, K. Niedenzu, J. Dawson, The vibrational spectrum of ethylene glycol, *Spectrochimica Acta Part A: Molecular Spectroscopy*, 23 (1967) 799-806.
- [37] K.L. Kelly, E. Coronado, L.L. Zhao, G.C. Schatz, The optical properties of metal nanoparticles: the influence of size, shape, and dielectric environment, *The Journal of Physical Chemistry B*, 107 (2003) 668-677.
- [38] S. Park, J. An, I. Jung, R.D. Piner, S.J. An, X. Li, A. Velamakanni, R.S. Ruoff, Colloidal suspensions of highly reduced graphene oxide in a wide variety of organic solvents, *Nano letters*, 9 (2009) 1593-1597.
- [39] L. Malard, M. Pimenta, G. Dresselhaus, M. Dresselhaus, Raman spectroscopy in graphene, *Physics Reports*, 473 (2009) 51-87.
- [40] G. Zhou, D.-W. Wang, L.-C. Yin, N. Li, F. Li, H.-M. Cheng, Oxygen bridges between NiO nanosheets and graphene for improvement of lithium storage, *ACS nano*, 6 (2012) 3214-3223.
- [41] T. Chen, F. Deng, J. Zhu, C. Chen, G. Sun, S. Ma, X. Yang, Hexagonal and cubic Ni nanocrystals grown on graphene: phase-controlled synthesis, characterization and their enhanced microwave absorption properties, *Journal of Materials Chemistry*, 22 (2012) 15190-15197.
- [42] K.N. Kudin, B. Ozbas, H.C. Schniepp, R.K. Prud'Homme, I.A. Aksay, R. Car, Raman spectra of graphite oxide and functionalized graphene sheets, *Nano letters*, 8 (2008) 36-41.
- [43] S. Guo, D. Wen, Y. Zhai, S. Dong, E. Wang, Platinum nanoparticle ensemble-on-graphene hybrid nanosheet: one-pot, rapid synthesis, and used as new electrode material for electrochemical sensing, *ACS nano*, 4 (2010) 3959-3968.
- [44] S. Park, K.-S. Lee, G. Bozoklu, W. Cai, S.T. Nguyen, R.S. Ruoff, Graphene oxide papers modified by divalent ions—enhancing mechanical properties via chemical cross-linking, *ACS nano*, 2 (2008) 572-578.
- [45] B. Li, H. Cao, ZnO@ graphene composite with enhanced performance for the removal of dye from water, *Journal of Materials Chemistry*, 21 (2011) 3346-3349.
- [46] P. Kundu, C. Nethravathi, P.A. Deshpande, M. Rajamathi, G. Madras, N. Ravishankar, Ultrafast microwave-assisted route to surfactant-free ultrafine Pt nanoparticles on graphene: synergistic co-reduction mechanism and high catalytic activity, *Chemistry of Materials*, 23 (2011) 2772-2780.

- [47] M.C. Biesinger, B.P. Payne, L.W. Lau, A. Gerson, R.S.C. Smart, X-ray photoelectron spectroscopic chemical state quantification of mixed nickel metal, oxide and hydroxide systems, *Surface and Interface Analysis*, 41 (2009) 324-332.
- [48] J. Wang, W. Bao, L. Zhang, A nonenzymatic glucose sensing platform based on Ni nanowire modified electrode, *Analytical Methods*, 4 (2012) 4009-4013.
- [49] C.E. Banks, R.R. Moore, T.J. Davies, R.G. Compton, Investigation of modified basal plane pyrolytic graphite electrodes: definitive evidence for the electrocatalytic properties of the ends of carbon nanotubes, *Chemical Communications*, (2004) 1804-1805.
- [50] X. Huang, Z. Yin, S. Wu, X. Qi, Q. He, Q. Zhang, Q. Yan, F. Boey, H. Zhang, Graphene-based materials: synthesis, characterization, properties, and applications, *small*, 7 (2011) 1876-1902.
- [51] S. Ramakrishna, K. Fujihara, W.-E. Teo, T. Yong, Z. Ma, R. Ramaseshan, Electrospun nanofibers: solving global issues, *Materials today*, 9 (2006) 40-50.
- [52] S. Bai, X. Shen, Graphene-inorganic nanocomposites, *Rsc Advances*, 2 (2012) 64-98.
- [53] D. Du, Y. Yang, Y. Lin, Graphene-based materials for biosensing and bioimaging, *MRS bulletin*, 37 (2012) 1290-1296.
- [54] B. Yuan, C. Xu, D. Deng, Y. Xing, L. Liu, H. Pang, D. Zhang, Graphene oxide/nickel oxide modified glassy carbon electrode for supercapacitor and nonenzymatic glucose sensor, *Electrochimica acta*, 88 (2013) 708-712.
- [55] Y. Yang, A.M. Asiri, Z. Tang, D. Du, Y. Lin, Graphene based materials for biomedical applications, *Materials today*, 16 (2013) 365-373.
- [56] H. Yoon, S. Ko, J. Jang, Field-effect-transistor sensor based on enzyme-functionalized polypyrrole nanotubes for glucose detection, *The Journal of Physical Chemistry B*, 112 (2008) 9992-9997.
- [57] A.D. Becke, K.E. Edgecombe, A simple measure of electron localization in atomic and molecular systems, *The Journal of chemical physics*, 92 (1990) 5397-5403.
- [58] W. Tang, E. Sanville, G. Henkelman, A grid-based Bader analysis algorithm without lattice bias, *Journal of Physics: Condensed Matter*, 21 (2009) 084204.
- [59] W. Orville-Thomas, *Atoms in Molecules—a Quantum Theory*: Richard FW Bader, Clarendon Press, Oxford, UK 1994, 438 pp., £ 25, Elsevier, 1996.
- [60] S. Sahoo, M.E. Gruner, S.N. Khanna, P. Entel, First-principles studies on graphene-supported transition metal clusters, *The Journal of chemical physics*, 141 (2014) 074707.

Figure captions

Figure. 1. Schematic illustrating the synthesis of Ni-NPs via a one-step polyol approach at low temperature and the formation of Ni-NPs/rGO on a GCE.

Figure. 2. Characterization of Ni-NPs. (a) XRD pattern of Ni-NPs. (b) FTIR spectrum of Ni-NPs. (c) SEM image of Ni-NPs. (d) DLS spectrum of Ni-NPs indicating the average nanoparticle size.

Figure. 3. Characterization of Ni-NPs/rGO. (a) XRD pattern of GO, rGO, and Ni-NPs/rGO. (b) Raman spectra of GO, rGO, and Ni-NPs/rGO. (c) SEM images of 42% Ni-NPs/rGO. (d) EDS mapping of 0.42% Ni-NPs/rGO showing the distribution of Ni-NPs within rGO nanosheets.

Figure. 4. (a) XPS survey spectra for core of elemental composition (b) C 1s (c) O 1s, and (d) Ni 2p states of Ni-rGO hybrid. Curve fittings were applied for the deconvolution analysis of (e) C 1s, and (f) Ni 2p_{3/2}.

Figure. 5. CVs of GCE, rGO, and Ni-NPs in the absence (a) and presence of 1 mM glucose (c). CVs of Ni-NPs/rGO on a GCE in 0.1 M NaOH solution in the absence (b) and presence of 1 mM glucose (d). (e) Schematic illustrating the electrochemical behavior of Ni-NPs/rGO sensor in the presence of glucose.

Figure. 6. Differential pulse voltammetry (DPV) diagram and calibration curve of 0.42% Ni-NPs/rGO in 0.1 M NaOH solution containing 0.25 μ M to 1.2 mM glucose (a and b, respectively).

Figure. 7. DFT calculation results for elucidating the molecular interactions of glucose with Ni-NPs/rGO. (a) Adsorption energy on Gr for different adsorbed molecules. (b) electron localization function maps on (110) plan of (b) Ni₁₃ nanocluster adsorbed on pristine Gr, and (c) glucose molecule adsorbed on Gr via assistance of Ni₁₃ nanocluster.

Figure 1

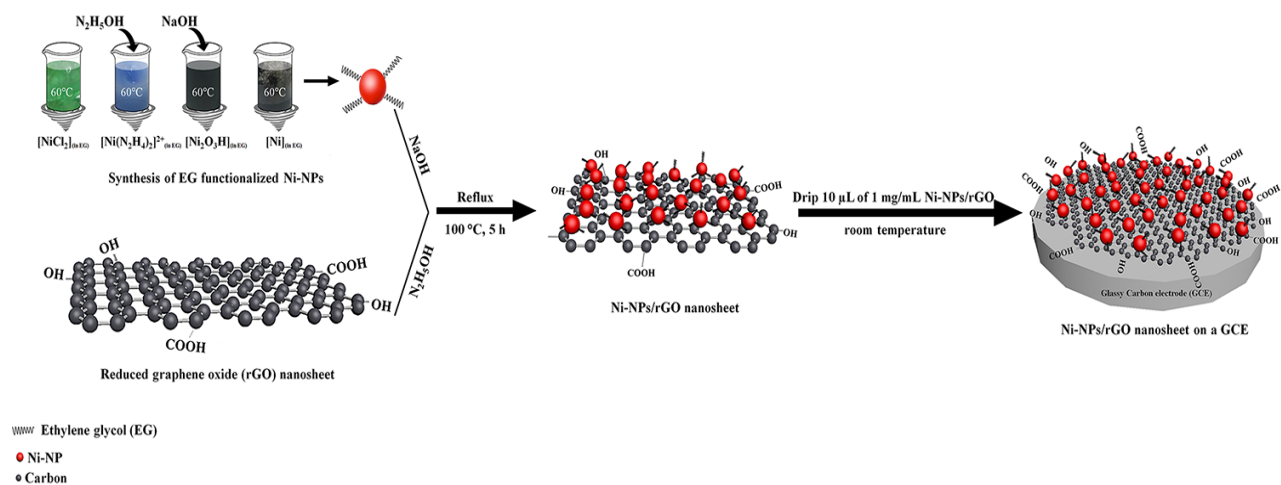


Figure 2

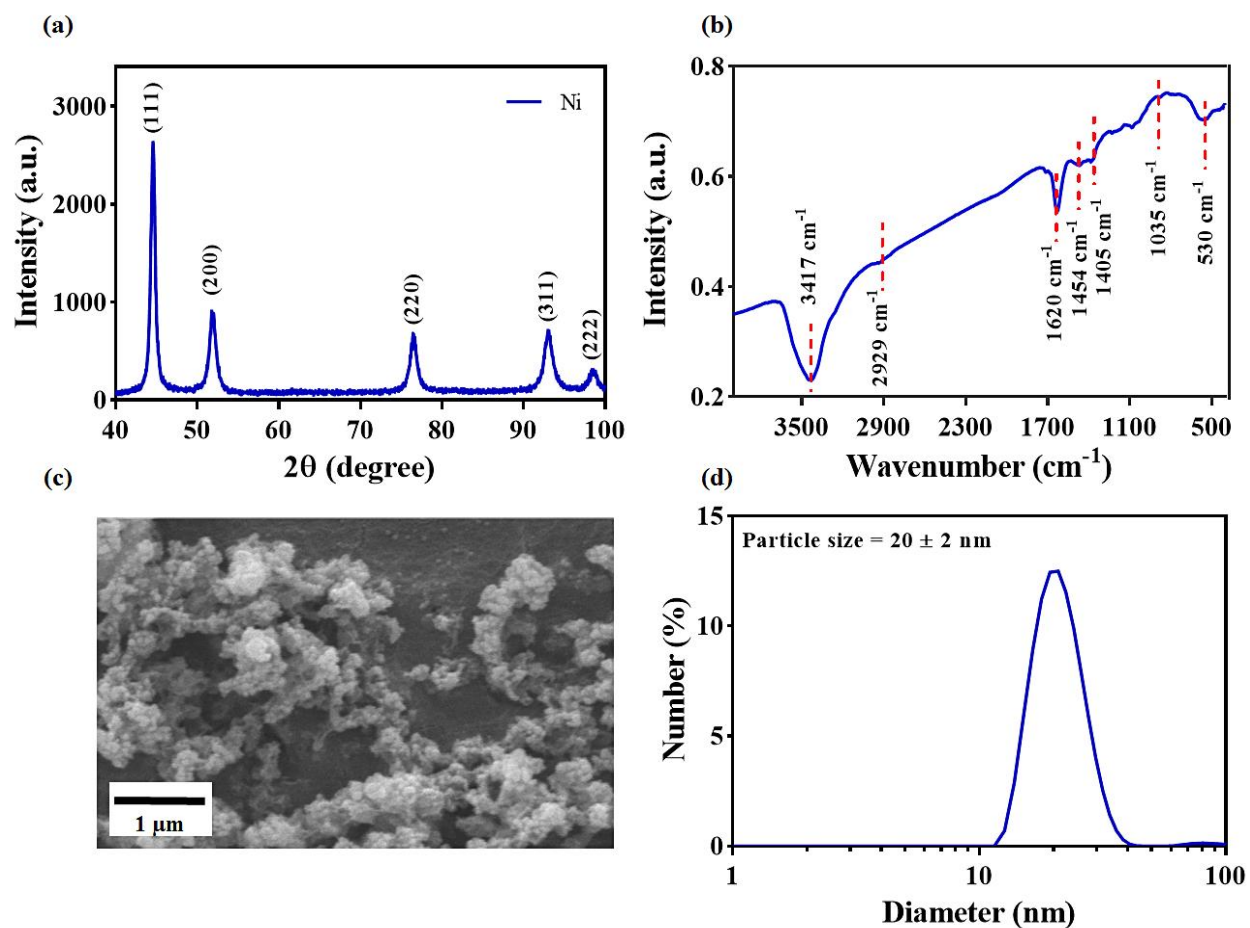


Figure 3

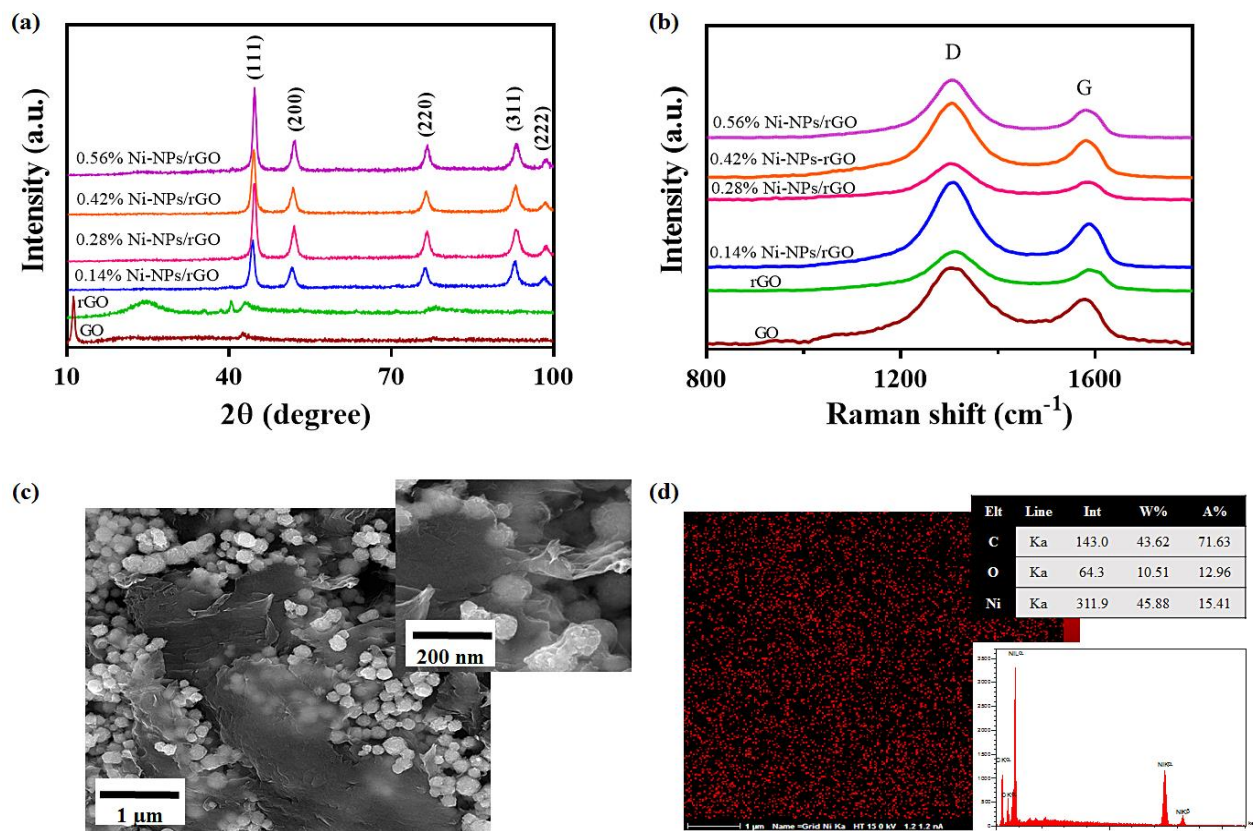


Figure 4

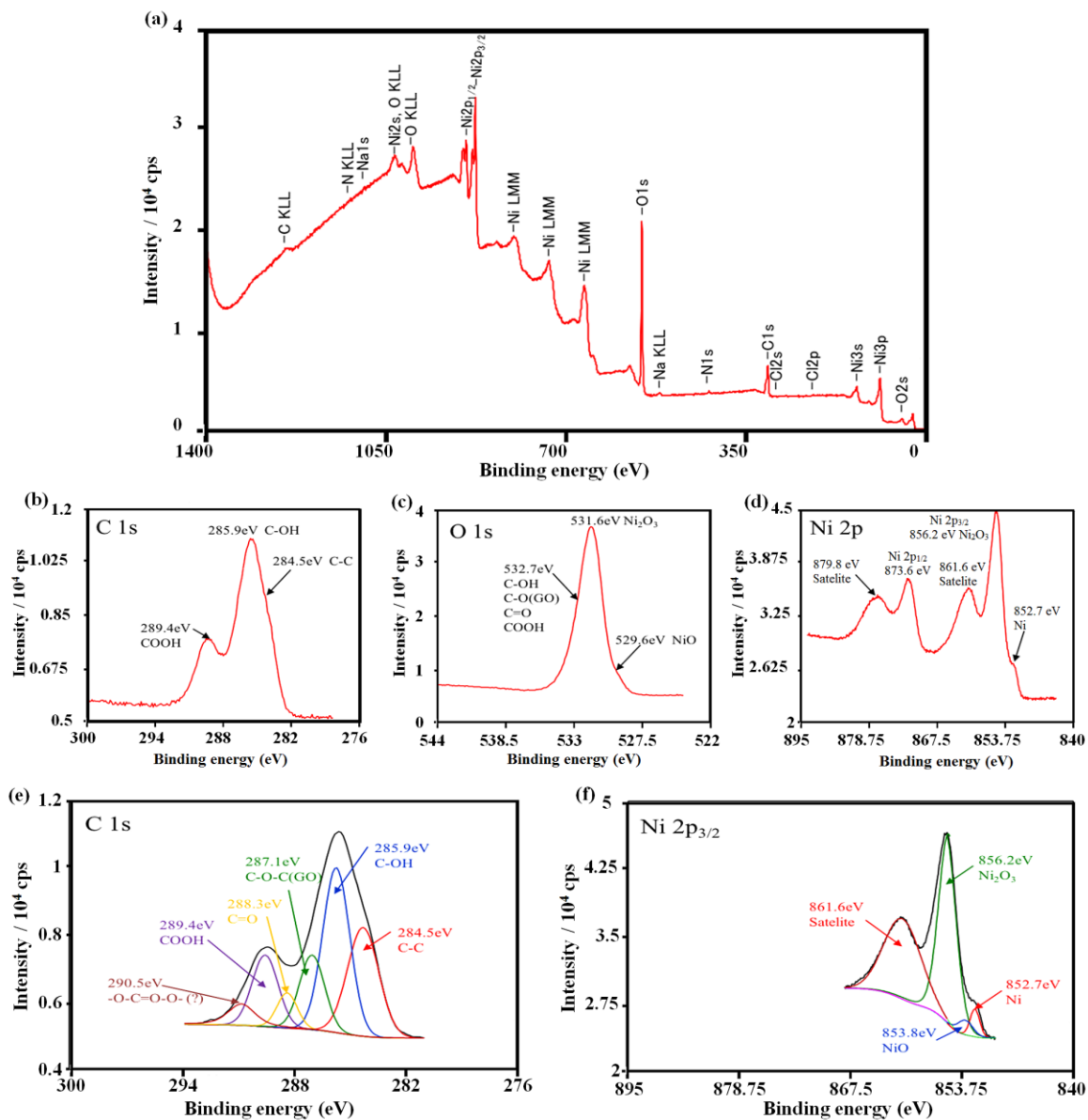


Figure 5

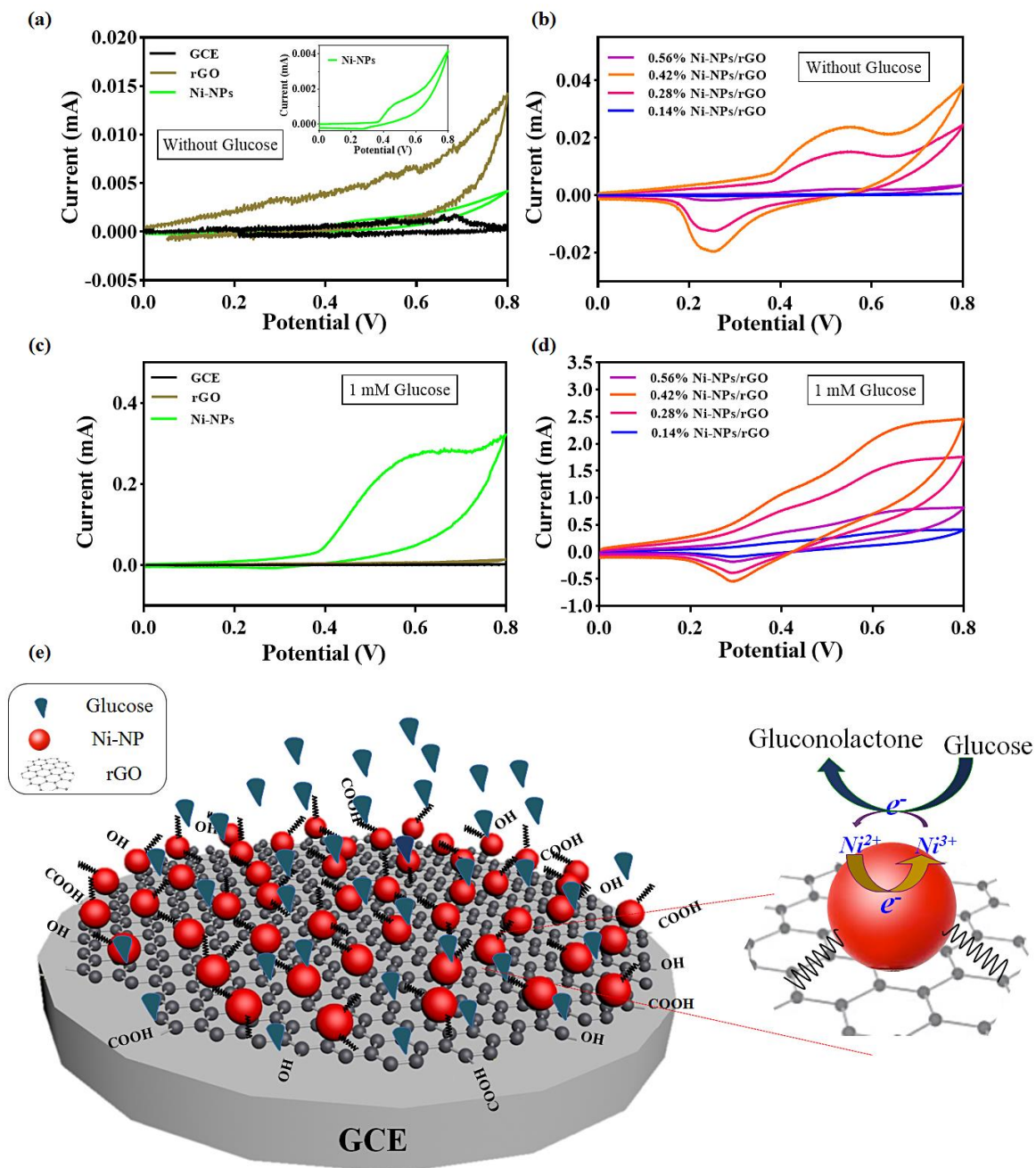


Figure 6

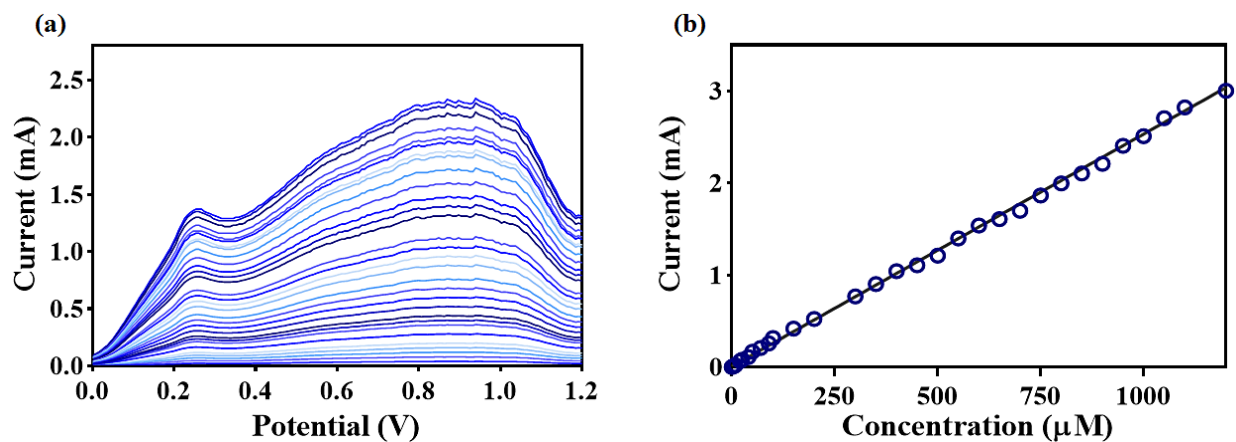


Figure 7

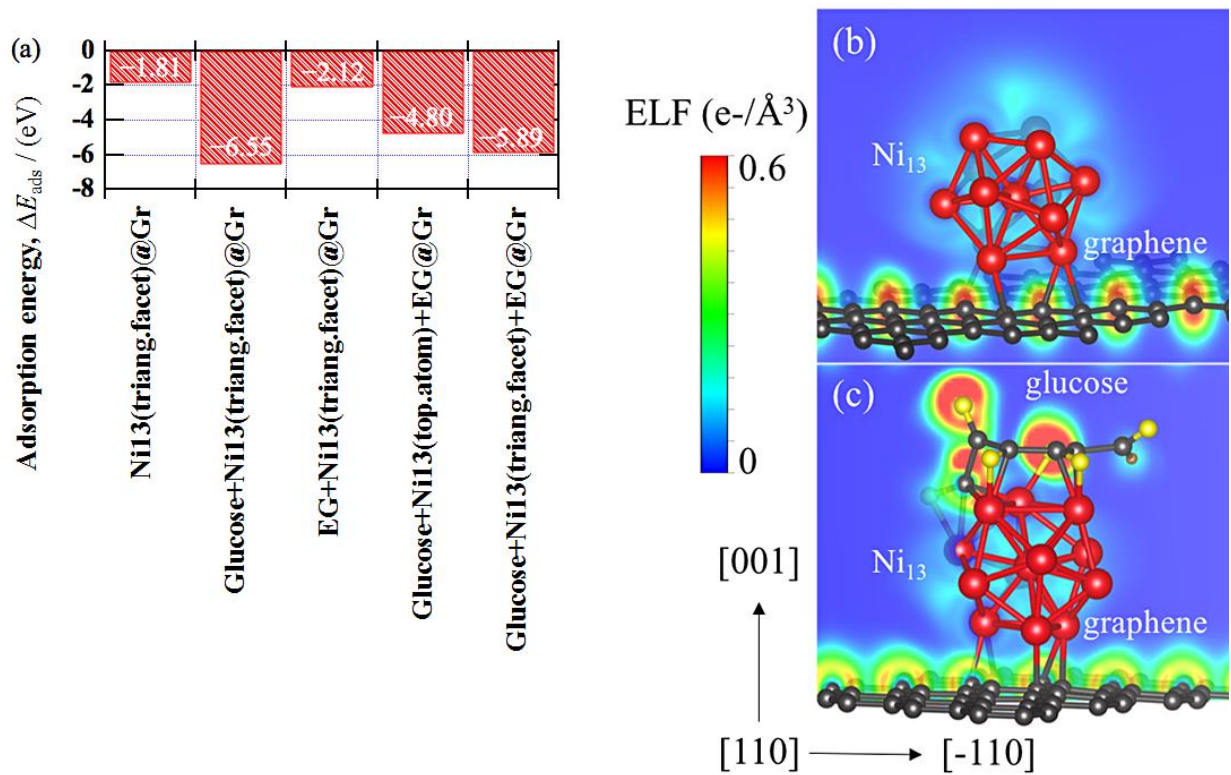


Table 1. C, O, and Ni content (at.%) of Ni-rGO (0.56 wt% Ni) sample based on XPS analysis.

Sample	C	N	O	Na	Cl	Ni
Ni-rGO	28.5	1.3	50.2	0.2	0.2	19.6

Table 2. Local magnetic moments (μ_B). The number of valance electrons are 4, 6, and 10 for C:($2s^22p^2$), O:($2s^22p^4$), and Ni:($3d^94s^1$), respectively.

Structure	No. of electrons	Local magnetic moment, M (μ_B)			
		$\langle M_{Ni} \rangle$	$\langle M_C \rangle$	$\langle M_O \rangle$	M_{tot}
Ni ₁₃ (triang.facet) @Gr	386	0.344 [‡]	-0.003	-	8.000
Glucose+Ni ₁₃ (triang.facet) @Gr	447	0.241 [*]	-0.001 [*]	-	5.001
		0.022 [‡]	-0.016 [‡]		
EG+Ni ₁₃ (triang.facet) @Gr	412	1.045 [†]	0.000 [†]	0.002	7.999
		0.060 [‡]	0.001 [‡]		
Glucose+Ni ₁₃ (top.atom)+EG @Gr	473	1.494 [*]	-0.009 [*]	0.001 ^G	9.032
		0.070 [†]	0.000 [†]	0.000 ^{EG}	
		0.000 [‡]	0.000 [‡]		
Glucose+Ni ₁₃ (triang.facet)+EG @Gr	473	0.387 [*]	-0.022 [*]	0.020 ^G	6.993
		0.776 [†]	0.013 [†]	0.002 ^{EG}	
			0.000 [‡]		

The symbols: * indicates values of the nearest neighbor Ni or C to glucose molecule, [†] nearest neighbors to EG, and [‡] nearest neighbors to Gr sheet. Values of O atoms of glucose, and EG molecules, are marked by superscripts G and EG.

Table 3. Bader charges (q^B) of elemental species in each configuration. The number of valence electrons are 4, 6, and 10 for C:($2s^22p^2$), O:($2s^22p^4$), and Ni:($3d^94s^1$), respectively.

Structure	No. of electrons	Bader charges (e)		
		$\langle q_{Ni}^B \rangle$	$\langle q_C^B \rangle$	$\langle q_O^B \rangle$
Ni₁₃(triang.facet)@Gr	386	9.743 [‡]	4.065	-
Glucose+Ni₁₃(triang.facet)@Gr	447	9.745*	4.179*	7.662
		9.531 [‡]	2.871 [‡]	
EG+Ni₁₃(triang.facet)@Gr	412	9.852 [†]	4.520 [†]	7.154
		9.746 [‡]	4.100 [‡]	
Glucose+Ni₁₃(top.atom)+EG@Gr	473	9.472*	3.002*	7.179 ^G
		9.658 [†]	3.969 [†] 3.988 [‡]	7.371 ^{EG}
Glucose+Ni₁₃(triang.facet)+EG@Gr	473	9.657*	2.640*	7.573 ^G
		9.700 [†]	3.783 [†] 3.992 [‡]	7.657 ^{EG}

The symbols: * indicates values of the nearest neighbor Ni or C to glucose molecule, [†] nearest neighbors to EG, and [‡] nearest neighbors to Gr sheet. Values of O atoms of glucose, and EG molecules, are marked by superscripts G and EG.